# Enhanced hydrological cycle increases ocean heat uptake and moderates transient climate sensitivity

Maofeng Liu[1*], Gabriel Vecchi[2,3], Brian Soden[1], Wenchang Yang[2], Bosong Zhang[1]

[1]Rosenstiel School of Marine and Atmospheric Science, University of Miami, Miami, FL

[2]Department of Geosciences, Princeton University, Princeton, NJ

[3]Princeton Environmental Institute, Princeton University, Princeton, NJ

Nov 19, 2020

[*]Corresponding Author: Maofeng Liu (mxl1744@miami.rsmas.edu; maofengliu2012@gmail.com)

This manuscript is a non-peer reviewed preprint submitted to EarthArXiv.

## Abstract

The large-scale moistening of the atmosphere in response to the greenhouse gas increases tends to amplify the existing patterns of precipitation minus evaporation (P-E) which, in turn, amplifies the spatial contrast in sea surface salinity (SSS). We propose that subtropical surface salinification due to the intensified hydrological cycle provides a buoyancy sink that increases the rate of ocean heat uptake and moderates transient climate sensitivity. We quantify the impact of these SSS changes in a series of $CO_2$ doubling experiments using two configurations of a coupled climate model: a standard configuration and a modified one in which SSS is held constant by restoring it back to its seasonally-varying climatology from the control run. In response to $CO_2$-induced warming, dry conditions (P-E < 0) over the subtropical oceans are amplified due to an enhanced hydrological cycle, increasing the SSS in salty regions. There is an increased rate of ocean heat uptake in the standard $CO_2$ doubling experiment relative to the fixed-SSS version. The largest increase in ocean heat content (OHC) for the standard run occurs in the southern subtropical Pacific and the tropical and subtropical Atlantic Ocean, where SSS shows the largest increase, highlighting the role of salinification in accelerating heat uptake. The weakening of the Atlantic Meridional Overturning Circulation in response to high latitude freshening and warming also plays a role in modulating the OHC. Consistent with a smaller rate of ocean heat uptake, the fixed-SSS version produces a transient climate response approximately 0.4K greater than the standard run. Observed multi-decadal changes in subsurface temperature and salinity resembles those simulated, indicating that anthropogenically-forced changes in salinity are likely enhancing the rate of ocean heat uptake.

## Main

The increased concentration of atmospheric greenhouse gases has reduced the longwave cooling of the Earth's climate system to space, resulting in planetary warming, which works to eventually bring the climate towards a new – warmer – equilibrium. It has been estimated that over 90% of the top-of-atmosphere energy imbalance is captured by oceans as increased ocean heat content (OHC)[1,2]. The resulting upper ocean warming can enhance the thermal stratification of oceans[3], and thus act to dampen mode water formation[4]. A recent study summarizing observation-based OHC estimates[5–7] and climate model simulations from the Coupled Model Intercomparison Project 5 (CMIP5)[8] claims a stronger rate of ocean warming over the period of 2005-2017 (0.54-0.64 W $m^{-2}$) relative to the period of 1971-2010 (0.36-0.39 W $m^{-2}$)[1]. Furthermore, in both observationally constrained OHC data[9] and climate model simulations[10], a substantial portion of increased OHC is found in tropics and subtropics (i.e., equatorward of 40$^o$ latitude). This creates a conundrum: given the stably stratified low-latitude oceans, how does the warming water get subducted to produce subtropical ocean heat uptake in spite of further stabilization from upper ocean warming[3,11]?

We propose that the amplification of the spatial pattern of sea surface salinity (SSS)[12–16] resulting from the enhancement of global hydrological cycle[17] provides an important supporting mechanism for the rate of ocean heat uptake. A robust consequence of anthropogenic warming is the increase of atmospheric moisture content controlled by the Clausius-Clapeyron (CC) relation, leading to the strengthening of the water cycle expressed as the amplification of the existing patterns of surface freshwater fluxes [precipitation minus evaporation (P – E)][17]. The enhancement of P – E amplifies the mean state, that is, "dry gets drier and wet gets wetter"[17]. Since SSS in part reflects large-scale patterns of P – E, the enhancement of the global hydrological cycle acts to amplify patterns of SSS: “fresh gets fresher and salty gets saltier”[12,13,18]. Analyses of long-term observations of SSS have revealed that the spatial changes of SSS largely resemble the climatological SSS distribution[12]. We hypothesize that salinification of the subtropical surface ocean provides an important buoyancy sink that helps compensate the stabilizing impact of upper ocean warming and enhance low-latitude heat uptake, and thus the enhancement of the hydrological cycle moderates transient climate sensitivity.

In this study, we quantify the impact of the sea surface salinification arising from an intensification of the global hydrological cycle on ocean heat uptake and transient climate sensitivity through a suite of transient $CO_2$ doubling experiments (i.e., atmospheric $CO_2$ concentration is increased at 1% per year until doubling). We compare the $CO_2$ response ($CO_2$-doubling minus control) in two configurations of a global coupled ocean-atmosphere climate model (FLOR)[10,19]: a standard configuration (labelled as STD), and a modified one nudging global SSS to the standard models’ seasonally-varying control climatology so that SSS is not allowed to freely evolve and thus respond to $CO_2$ forcing (labelled as fixed-SSS-GL; see Methods for details). Differences in $CO_2$ response between these two configurations highlight the influences of SSS changes on transient climate sensitivity.

Compared to the STD version, the fixed-SSS-GL version shows a greater increase of global mean surface temperature with a larger transient climate response (TCR) by 0.4 K, highlighting the role of $CO_2$-induced SSS changes in reducing the rate of surface warming in response to $CO_2$ doubling (Fig. 1). The climatological effect of fixing SSS on unforced simulations of surface temperature, examined by comparing the 100-year control runs from both the standard FLOR and the version with fixed SSS, is relatively small (0.002 K over the 100-year period as seen in Supplementary Fig. S1).

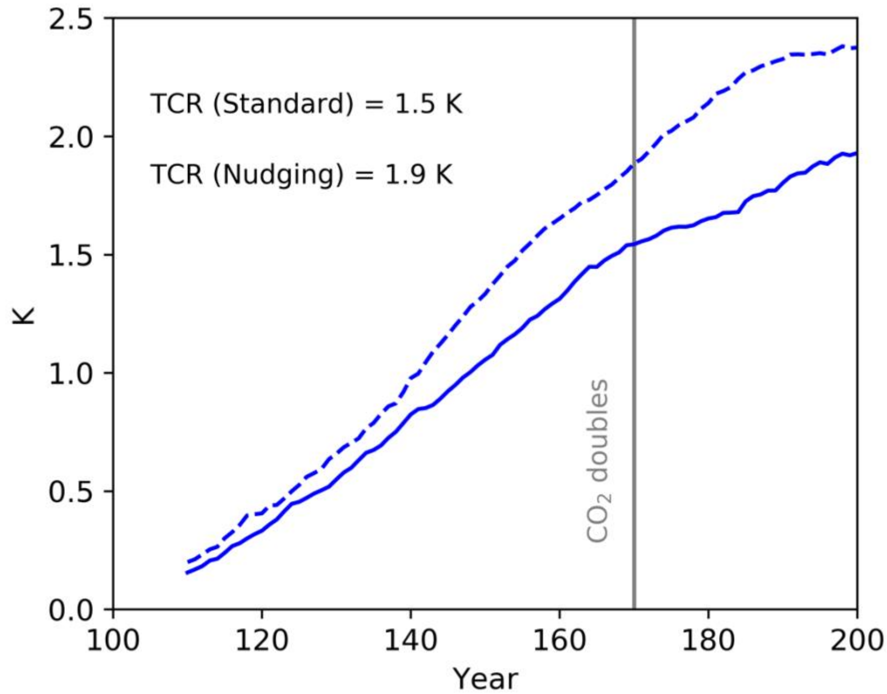


Fig. 1. Time series of global mean surface temperature changes (ºC) in response to a 1% annual increase in $CO_2$ concentration for (solid) the STD and (dashed) fixed-SSS-GL version. Data are plotted as 20-year running mean.

The greater surface warming in the fixed-SSS-GL experiment relative to the STD run, given the similar climate feedback parameter (1.6 and 1.5 W $m^{-2}$ $K^{-1}$ for the STD and fixed-SSS-GL version, respectively; see Methods for details), should result in a larger radiative response of the climate system. Based on the top-of-atmosphere (TOA) energy balance [$R(t) = Q(t) – \lambda\Delta T(t)$ where R is the net radiation at the TOA, Q is the radiative forcing, $\lambda$ is the climate feedback parameter, $\Delta T$ is the surface warming and t is time], a lower radiative imbalance at the TOA occurs when SSS is fixed given the same $CO_2$-induced radiative forcing (Fig. 2a). This indicates the fixed-SSS-GL version has a much lower ocean heat uptake efficiency[20,21], defined as the ratio of net radiation at the TOA to the global surface temperature increase. Consistently, the fixed-SSS-GL experiment shows a smaller increase of OHC in comparison with the standard experiment (Fig. 2a). It is worth noting that the effect of nudging SSS on unforced simulations of net radiation at the TOA and OHC, similar to global mean surface temperature (Supplementary Fig. S1), is small (Supplementary Fig. S2).

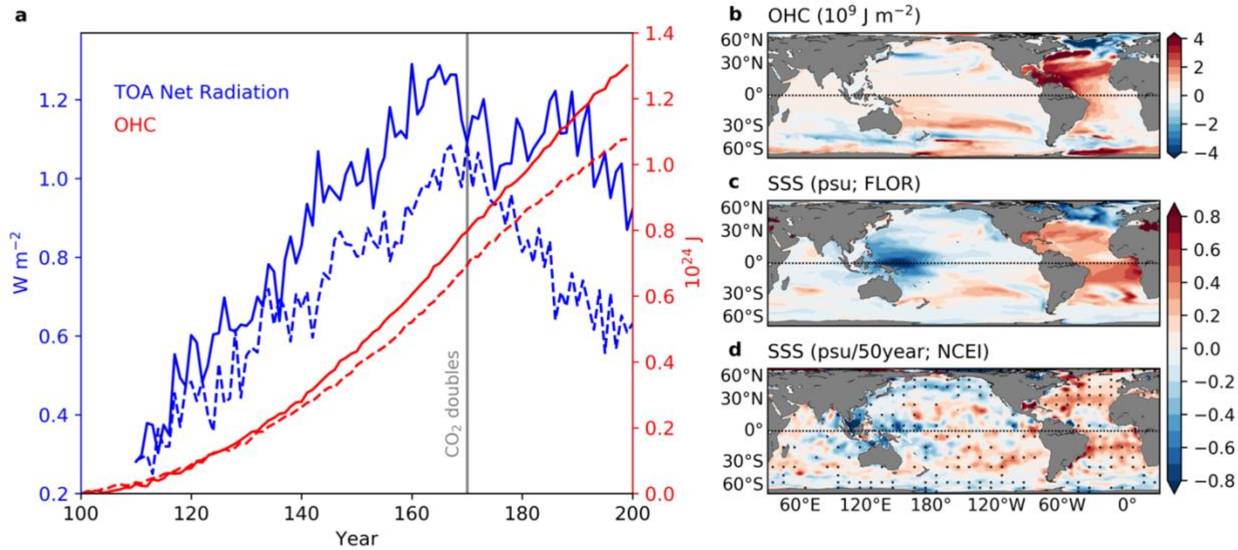


Fig. 2. **a**. Annual series of changes in (blue) top-of-atmosphere (TOA) net radiation (W $m^{-2}$) and (red) ocean heat content (OHC; $10^{24}$ J) in response to a 1% annual increase in $CO_2$ for (solid line) the STD and (dashed line) fixed-SSS-GL version. The grey line indicates year 170 when the $CO_2$ doubles. The TOA net radiation is plotted as 10-year running mean. **b**. Difference in the response of OHC ($10^9$ J $m^{-2}$) to $CO_2$ doubling between the STD and fixed-SSS-GL version. The difference is computed using years 161-180 for the $CO_2$ run while years 101-200 for the control run. **c**. The same as **b**. but for difference in the response of sea surface salinity (SSS; psu). **d**. The linear trend of SSS (psu/50yr) from NCEI data over the period of 1968-2017. The trend is tuned by the ratio of $CO_2$ concentration at $CO_2$ doubling in FLOR to that in 2017 from observations. The area with statistical significance ($p < 0.05$) is stippled.

The STD version shows a greater increase of ocean heat uptake in response to the $CO_2$ forcing, relative to the fixed-SSS-GL version (Fig. 2b). The greatest increase occurs in the tropical and subtropical Atlantic Ocean and secondly in the subtropical South Pacific (Fig. 2b), broadly mirroring regions where SSS shows the largest increase[22] (Fig. 2c). The results support our hypothesis on the role of sea surface salinification in enhancing heat penetration into deeper oceans by reduced density stratification resulting from upper-ocean warming. The spatial distribution of SSS change in response to the $CO_2$ forcing (Fig. 2c) is broadly consistent with the change in P-E

(Supplementary Fig. S3a) strongly tied to the mean state (Supplementary Fig. S3b), echoing the impact of the amplified water cycle on surface salinity changes[12–14,17]. The linear trend of SSS from an observational data set spanning the period of 1968-2017 from National Centers for Environmental Information (NCEI)[9] resembles the spatial pattern of SSS change seen in the idealized FLOR experiments (Fig. 2d), a resemblance that is robust across different observationally-based ocean salinity data sets (Supplementary Fig. S4), suggesting the emergent signal of human-induced forcing in shaping the observed changes of ocean salinity, as identified by a number of recent studies[15,22,23].

Relative to the fixed-SSS-GL version, the STD version exhibits deeper warming (Fig. 3a): reduced increase of heating within the upper 300 m, in agreement with the reduced increase of surface temperature (Fig. 1). The downward shift of OHC arising from SSS changes is further evident in the zonally-integrated subsurface temperature in response to $CO_2$ doubling (Fig. 3c, e). It is worth noting that, relative to the zonal mean, the zonal integral provides a more relevant measure to compare tropics and subpolar regions by taking into account the difference in area per unit latitude at different latitudes related to both the convergence of meridians and differences in land mass. The Atlantic Ocean accounting for 54% of all heat increase and its greatest salinity-induced increase of subsurface temperature occurs in the northern subtropics where the increase of subsurface salinity also reaches its peak (Fig. 3b, c). For oceans other than the Atlantic, there is also correspondence between the positive anomaly of subsurface temperature and salinity, as shown in the southern subtropics, primarily in the Pacific Ocean (Fig. 3d, e). These results suggest the important role of the increased subsurface salinity in the subtropical oceans driven by surface salinification in modulating the vertical distribution of OHC through accelerated heat uptake. The wind-driven turbulent mixing in the upper layers seems to play a less important role in the difference in OHC response between the two versions: 1) the mixed layer depth in winter shows insignificant difference between the two versions of FLOR in subtropical oceans; 2) most of the extra heat sink is sequestrated deeper than the mixed layer depth (Fig. 3b-d). The intermediate layer (700-2000 m) sequesters more heat than other layers (Fig. 3a), in part driven by increased heat penetration associated with the positive salinity anomaly (Fig. 3b, d). The confinement of this salinity anomaly within the upper 1000 m (Fig. 3b, d) implies other mechanisms are needed to cause the extra heat increase in the lower portion of the intermediate layer.

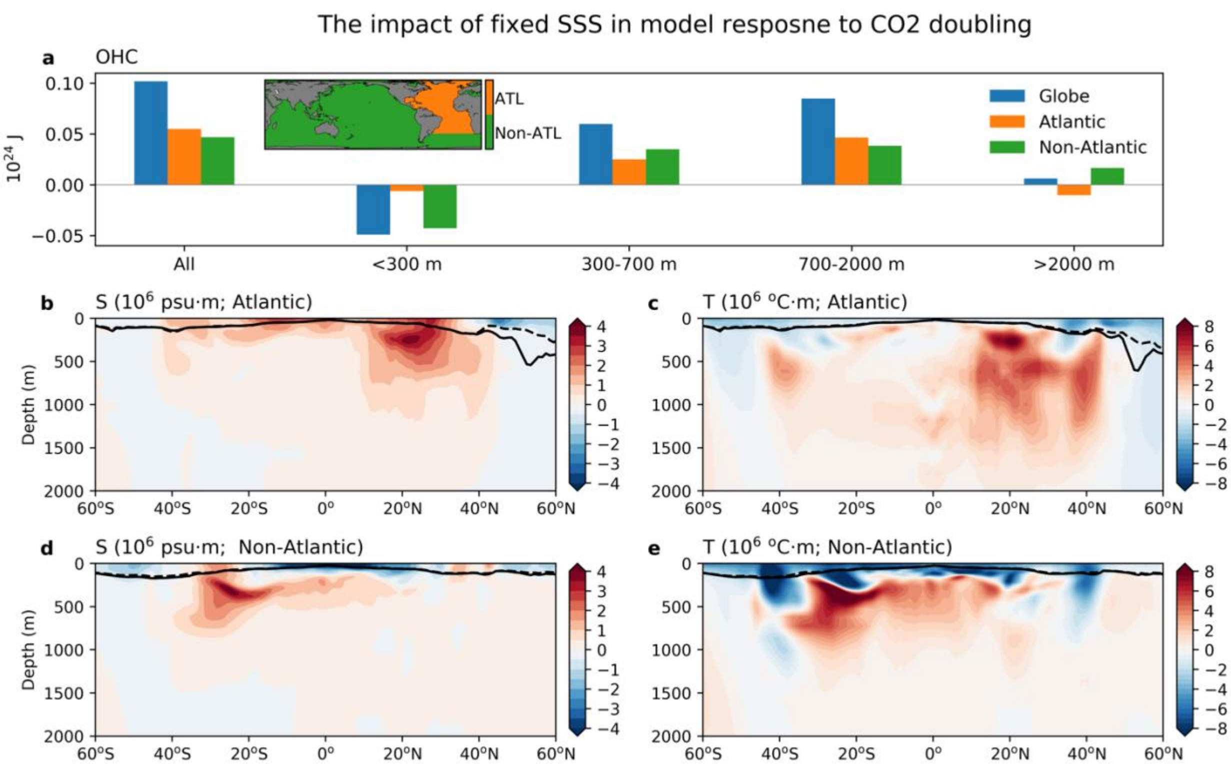


Fig. 3. **a**. Difference in the response of OHC ($10^{24}$ J) to transient $CO_2$ doubling between the STD and fixed-SSS-GL version as a function of ocean depth. The difference is computed using years 161-180 for the $CO_2$ run while years 101-200 for the control run. The inset figure indicates the area of Atlantic and non-Atlantic Oceans for computing total OHC. **b-c**. Difference in the response of zonal-integral **b** ocean salinity ($10^6$ psu·m; color) and **c** ocean temperature ($10^6$ °C·m; color) between the STD and fixed-SSS-GL version in the Atlantic using the same period as **a**. **d-e**. As in **b-c**, but non-Atlantic Oceans. Black lines in **b-d** indicate winter mixed layer depth (mld; m) from control runs (solid) and $CO_2$ runs (dashed), respectively. The mld in **b**, **d** are from the STD version while the mld in **c**, **e** are from the fixed-SSS-GL version.

Given the importance of the ocean circulation in driving heat transports and related temperature changes, we further investigated the role of the ocean circulation. Weakening of the Atlantic Meridional Overturning Circulation (AMOC) in response to greenhouse gas forcing, as seen in a number of previous studies[24–26], is seen in the idealized $CO_2$ doubling experiment with FLOR (Supplementary Fig. 5). The fixed-SSS-GL version produces less weakening of AMOC relative to the STD run, probably due to the suppression of the subpolar freshening by climatological SSS nudging[25]. The impact of the difference in AMOC change is explored by another set of experiments that only nudge SSS in the subtropical Atlantic (labelled as fixed-SSS-subAtl; Supplementary Fig. 6) to allow subpolar freshening. The fixed-SSS-subAtl version produces a similar AMOC weakening relative to the STD run, allowing us to distinguish the relative role of AMOC and salinification on OHC changes. In response to the $CO_2$ forcing, the STD version shows a greater increase of OHC by $4.1\times10^{22}$ J relative to the fixed-SSS-subAtl version in the Atlantic Ocean (Supplementary Fig. 7 a), accounting for 74% of that relative to the fixed-SSS-GL version. This heat anomaly overlaps with the positive salt anomaly in the subtropical North Atlantic (Supplementary Fig. 7 b-c), further implying the key role of salinification in accelerating heat uptake. In addition, the heat anomaly is primarily sequestrated in the upper ocean (< 700 m) (Supplementary Fig. 7 c), in contrast to the intermediate level (700-2000 m) for the heat anomaly between the STD and fixed-SSS-GL version (Fig. 3). These results suggest the role of ocean circulation in heat sequestration below upper oceans for the following reasons. First, the enhanced northward transport of salty water in the fixed-SSS-GL version relative to the other two experiments due to less AMOC weakening could lead to decreased salt in the subtropics and thus reduced heat sink to deeper levels. Second, the enhanced southward import of North Atlantic Deep Water in the fixed-SSS-GL version could transport more subpolar cold water to the intermediate level in the subtropics, resulting in less warming than the other two experiments. Besides fixed-SSS-subAtl, we conducted another set of experiments that partially nudged SSS in non-Atlantic oceans (labelled as fixed-SSS-nonAtl; Supplementary Fig. 8). The weakening of AMOC in the fixed-SSS-nonAtl version is closer the STD version than the fixed-SSS-GL version, resulting in reduced impact from AMOC on OHC changes (Supplementary Fig. 5). Outside of the Atlantic, the fixed-SSS-nonAtl version exhibits similar changes of OHC and subsurface temperature (Supplementary Fig. 9 a, e) to the fixed-SSS-GL version (Fig. 3 a, e), further demonstrating the important role of subtropical salinification (Fig. 3 d; Supplementary Fig. 9 d) in enhancing ocean heat uptake.

The simulated response of ocean subsurface temperature and salinity to the idealized $CO_2$ forcing from the STD version resembles many key features in the linear trend of observations spanning the period of 1968-2017 (Fig. 4), implying the likely emergent signal of human-induced forcing in driving the temperature and salinity changes[15,22,23,27]. This similarity is broadly robust across data sets (Supplementary Figs. 10-12).

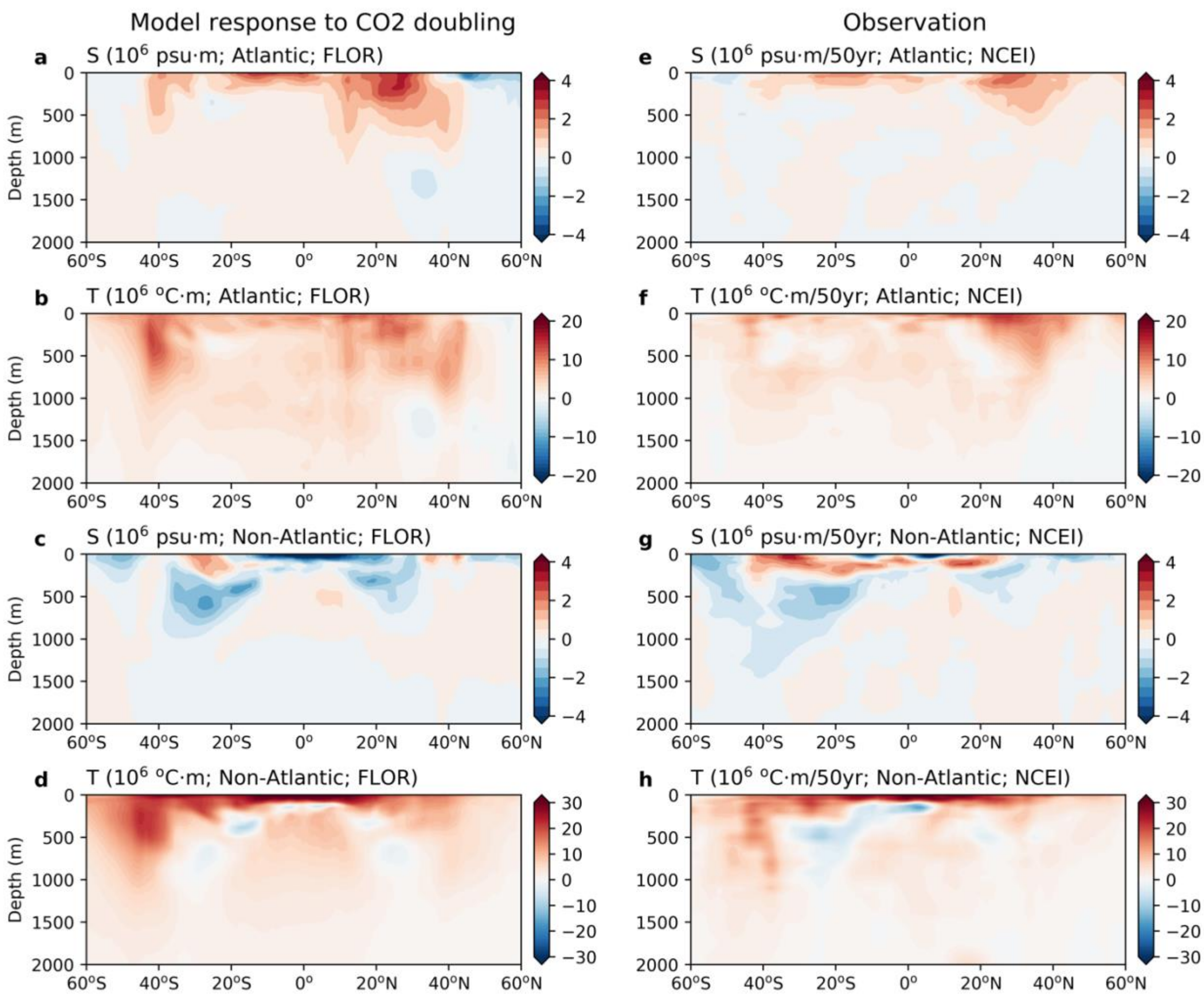


Fig. 4. **a-b**. Change in zonal-integral **a** ocean subsurface salinity ($10^6$ psu·m; color) and **b** ocean temperature ($10^6$ °C ·m; color) in response to transient $CO_2$ doubling in the Atlantic Ocean for the STD runs. **c-d**. As in **a-b**, but non-Atlantic Oceans. **e-h**. As in **a-d**, but the linear trend of ocean salinity ($10^6$ psu·m/50yr) and temperature ($10^6$ °C·m/50yr) from the NCEI data over the period of 1968-2017. The trend is tuned by the ratio of $CO_2$ concentration at $CO_2$ doubling in FLOR to that in 2017 from observations.

In the Atlantic Ocean, both the STD simulations and in situ data show a positive salt anomaly (Fig. 4a, e) overlapped with the heat anomaly (Fig. 4b, f) in the subtropics which, as demonstrated in the FLOR experiments, is primarily driven by subtropical surface salinification associated with intensified hydrological cycle. A major difference lies in the subpolar North Atlantic where the decrease of subsurface salinity and temperature in FLOR is less clear in observations, primarily driven by their difference in AMOC changes. AMOC weakening in response to $CO_2$ forcing in the standard FLOR experiment (Supplementary Fig. 5) is not seen in the past few decades due to strong decadal variability[28,29], although recent studies employing proxy data claimed the century-scale weakening of AMOC[30,31].

For oceans other than the Atlantic, both the STD simulations and observations show decreased salinity in the upper ocean extending to 1000 m in subtropics (Fig. 4 c, g), broadly overlapping with the warming hole (Fig. 4 d, h). Although the surface salinification in the south subtropics from the STD version does not exceed the rate of freshening beneath (Fig. 4c), it leads to more salt and heat penetration into deeper layers than the fixed-SSS-GL version in which the surface salinification is suppressed (Fig. 3 d-e). The 40$^o$-50$^o$S zone of the Southern Ocean shows substantial warming (Fig. 4 b, d), which is claimed in a recent work[32] to result from the northward heat transport associated with the Antarctic Circumpolar Current.

In this study, we highlight the previously overlooked role of subtropical salinification-driven by the enhanced water cycle[12–17] in response to greenhouse warming -in accelerating the rate of ocean heat uptake and thus moderating transient climate sensitivity. By a set of climate model experiments we demonstrate that, without the subtropical salinification, the transient climate response could increase by 0.4 K. This suggests that the multi-model spread in transient climate sensitivity may be partially traced to their spread in simulating ocean salinity. The increasing emergence of the anthropogenic signal in the ocean water masses[27] raises the need for future research of the competing mechanism between upper ocean warming and subtropical salinification in ocean stratification, which is critical for improved understanding of past and future ocean heat uptake and transient climate sensitivity.

## Method

We use the Forecast-oriented Low Ocean Resolution (FLOR) model (FLOR)[19,33] developed at Geophysical Fluid Dynamics Laboratory (GFDL). FLOR has a horizontal resolution of approximately 50 km for the atmosphere and land components developed from GFDL Coupled Model (CM) version 2.5 and a coarser (~1°) resolution for the oceanic and sea ice components from GFDL CM version 2.1. We use the FLOR model to conduct a set of fully-coupled experiments. The first experiment is labeled as a standard control simulation in which the radiative forcing and land use/land cover is maintained as the level of year 1990 for 200 years. The first 100 years were treated as model spin-up and discarded from further analyses. Beside the standard control simulation, we also carried out two control experiment in which the sea surface salinity (SSS) of the fully-coupled model is “nudged” to the climatological SSS over the global ocean (labeled as fixed-SSS-GL) and the subtropical Atlantic Ocean (Supplementary Fig. 6; labeled as fixed-SSS-subAtl), respectively, using model year 101 in the standard control simulation for the initial condition. Corresponding to each standard control simulation, we conducted a perturbation experiment in which the atmospheric $CO_2$ concentration was increased at a rate of 1% per year until doubling from year 101 (i.e., 100 years after model initialization), and was then held fixed.

For each experiment, the climate response to $CO_2$ doubling is computed as difference between model year 161-180 from the perturbation run and model year 101-200 from the control run.

We use four gridded data sets of ocean salinity and temperature for the period of 1968-2017. The first three data sets constructed based on in situ measurements are National Centers for Environmental Information (NCEI), United States[9], Japan Meteorological Agency (JMA), Japan[5] and Institute of Atmospheric Physics (IAP), China[6,34]. We also use an ocean reanalysis product from Ocean Reanalysis System 4 (ORAS4)[35] that constrains the model simulations with in situ measurements. The linear trend of ocean salinity and temperature spanning from 1968 to 2017 is computed using an ordinary least-square linear fit and then multiplied by 50 to represent changes. We tuned the trend before comparing it to FLOR-simulated change roughly by the ratio of $CO_2$ concentration at $CO_2$ doubling in FLOR to that in 2017 from observations.

We use the radiative kernel method[36] to calculate the transient radiative feedbacks for the $CO_2$ stabilization period (i.e., year 161-180). The radiative kernel for a feedback variable $x$ is defined as $K^x = \partial R/\partial x$, in which $R$ is the net top-of-atmosphere (TOA) flux, and x is an individual radiative state variable (e.g., temperature, water vapor, clouds, or surface albedo). The radiative kernel is derived from *CloudSat/CALIPSO* measurements[37,38].

**Acknowledgements**

This work was supported by Award 80NSSC20K0879 from the National Aeronautics and Space Administration and Award DE-SC0021333 from the U.S. Department of Energy. The simulations presented in this paper were performed on computational resources managed and supported by Princeton Research Computing at Princeton University. The climate model used in this study is GFDL FLOR with code available at the NOAA/GFDL website (https://www.gfdl.noaa.gov/cm2-5- and-flor/). The NCEI ocean salinity and temperature data is available at (https://www.nodc.noaa.gov/OC5/3M_HEAT_CONTENT/). The JMA data is available at (https://climate.mri-jma.go.jp/pub/ocean/ts/v7.3/). The IAP data is available at (http://159.226.119.60/cheng/). The ORAS4 data is available at (ftp://ftp-icdc.cen.uni-hamburg.de/EASYInit/ORA-S4/).

**Author contributions**

B.S., G.V. and M.L. designed the research; G.V., M.L. and W.Y. performed the simulations; M.L. performed analysis; M.L. wrote the draft; and all the authors contributed to the interpretation of the results and the writing of the paper.

**Competing interests**

The authors declare no competing financial interests.

## Reference

1. Cheng, L., Abraham, J., Hausfather, Z. & Trenberth, K. E. How fast are the oceans warming? *Science (80-. ).* **363**, 128 LP – 129 (2019).
2. Trenberth, K. E., Fasullo, J. T. & Balmaseda, M. A. Earth's energy imbalance. *J. Clim.* **27**, 3129–3144 (2014).
3. Li, G. *et al.* Increasing ocean stratification over the past half-century. *Nat. Clim. Chang.* (2020). doi:10.1038/s41558-020-00918-2
4. Stevens, S. W., Johnson, R. J., Maze, G. & Bates, N. R. A recent decline in North Atlantic subtropical mode water formation. *Nat. Clim. Chang.* **10**, (2020).
5. Ishii, M. *et al.* Accuracy of Global Upper Ocean Heat Content Estimation Expected from Present Observational Data Sets. *Sola* **13**, 163–167 (2017).
6. Cheng, L. *et al.* Improved estimates of ocean heat content from 1960 to 2015. *Sci. Adv.* **3**, 1–10 (2017).
7. Domingues, C. M. *et al.* Improved estimates of upper-ocean warming and multi-decadal sea-level rise. *Nature* **453**, 1090–1093 (2008).
8. Taylor, K. E., Stouffer, R. J. & Meehl, G. A. An Overview of CMIP5 and the Experiment Design. *Bull. Am. Meteorol. Soc.* **93**, 485–498 (2012).
9. Levitus, S. *et al.* World ocean heat content and thermosteric sea level change (0–2000 m), 1955–2010. *Geophys. Res. Lett.* **39**, (2012).
10. Vecchi, G. A. *et al.* Tropical cyclone sensitivities to CO2 doubling: roles of atmospheric resolution, synoptic variability and background climate changes. *Clim. Dyn.* (2019). doi:10.1007/s00382-019-04913-y
11. Capotondi, A., Alexander, M. A., Bond, N. A., Curchitser, E. N. & Scott, J. D. Enhanced

upper ocean stratification with climate change in the CMIP3 models. *J. Geophys. Res. Ocean.* **117**, 1–23 (2012).

12. Durack, P. J. & Wijffels, S. E. Fifty-Year trends in global ocean salinities and their relationship to broad-scale warming. *J. Clim.* **23**, 4342–4362 (2010).

13. Durack, P. J., Wijffels, S. E. & Matear, R. J. Ocean Salinities Reveal Strong Global Water Cycle Intensification During 1950 to 2000. *Science (80-. ).* **336**, 455 LP – 458 (2012).

14. Skliris, N. *et al.* Salinity changes in the World Ocean since 1950 in relation to changing surface freshwater fluxes. *Clim. Dyn.* **43**, 709–736 (2014).

15. Terray, L. *et al.* Near-surface salinity as nature's rain gauge to detect human influence on the Tropical water cycle. *J. Clim.* (2012). doi:10.1175/JCLI-D-10-05025.1

16. Lago, V. *et al.* Simulating the role of surface forcing on observed multidecadal upper-ocean salinity changes. *J. Clim.* (2016). doi:10.1175/JCLI-D-15-0519.1

17. Held, I. M. & Soden, B. J. Robust responses of the hydrological cycle to global warming. *J. Clim.* (2006). doi:10.1175/JCLI3990.1

18. Stocker, T. F. *et al. Climate change 2013 the physical science basis: Working Group I contribution to the fifth assessment report of the intergovernmental panel on climate change*. *Climate Change 2013 the Physical Science Basis: Working Group I Contribution to the Fifth Assessment Report of the Intergovernmental Panel on Climate Change* (2013). doi:10.1017/CBO9781107415324

19. Vecchi, G. A. *et al.* On the Seasonal Forecasting of Regional Tropical Cyclone Activity. *J. Clim.* **27**, 7994–8016 (2014).

20. Gregory, J. M. & Mitchell, J. F. B. The climate response to CO2 of the Hadley Centre coupled AOGCM with and without flux adjustment. *Geophys. Res. Lett.* (1997).

doi:10.1029/97GL01930

21. Raper, S. C. B., Gregory, J. M. & Stouffer, R. J. The role of climate sensitivity and ocean heat uptake on AOGCM transient temperature response. *J. Clim.* (2002). doi:10.1175/1520-0442(2002)015<0124:trocsa>2.0.co;2

22. Stott, P. A., Sutton, R. T. & Smith, D. M. Detection and attribution of Atlantic salinity changes. *Geophys. Res. Lett.* (2008). doi:10.1029/2008GL035874

23. Pierce, D. W., Gleckler, P. J., Barnett, T. P., Santer, B. D. & Durack, P. J. The fingerprint of human-induced changes in the ocean's salinity and temperature fields. *Geophys. Res. Lett.* **39**, 2–7 (2012).

24. Stouffer, R. J. *et al.* Investigating the cause of the response of the thermohaline circulation to past and future climage changes. *J. Clim.* **19**, 1365–1387 (2006).

25. Liu, W., Fedorov, A. V, Xie, S.-P. & Hu, S. Climate impacts of a weakened Atlantic Meridional Overturning Circulation in a warming climate. *Sci. Adv.* **6**, eaaz4876 (2020).

26. Levang, S. J. & Schmitt, R. W. What Causes the AMOC to Weaken in CMIP5? *J. Clim.* **33**, 1535–1545 (2019).

27. Silvy, Y., Guilyardi, E., Sallée, J.-B. & Durack, P. J. Human-induced changes to the global ocean water masses and their time of emergence. *Nat. Clim. Chang.* (2020). doi:10.1038/s41558-020-0878-x

28. Robson, J., Ortega, P. & Sutton, R. A reversal of climatic trends in the North Atlantic since 2005. *Nat. Geosci.* **9**, 513–517 (2016).

29. Jackson, L. C., Peterson, K. A., Roberts, C. D. & Wood, R. A. Recent slowing of Atlantic overturning circulation as a recovery from earlier strengthening. *Nat. Geosci.* **9**, 518–522 (2016).

30. Thornalley, D. J. R. *et al.* Anomalously weak Labrador Sea convection and Atlantic overturning during the past 150 years. *Nature* **556**, 227–230 (2018).

31. Caesar, L., Rahmstorf, S. & Feulner, G. On the relationship between Atlantic meridional overturning circulation slowdown and global surface warming. *Environ. Res. Lett.* **15**, 24003 (2020).

32. Armour, K. C., Marshall, J., Scott, J. R., Donohoe, A. & Newsom, E. R. Southern Ocean warming delayed by circumpolar upwelling and equatorward transport. *Nat. Geosci.* (2016). doi:10.1038/ngeo2731

33. Jia, L. *et al.* Improved Seasonal Prediction of Temperature and Precipitation over Land in a High-Resolution GFDL Climate Model. *J. Clim.* **28**, 2044–2062 (2015).

34. Cheng, L. *et al.* Improved estimates of changes in upper ocean salinity and the hydrological cycle. *J. Clim.* 1–74 (2020). doi:10.1175/JCLI-D-20-0366.1

35. Balmaseda, M. A., Mogensen, K. & Weaver, A. T. Evaluation of the ECMWF ocean reanalysis system ORAS4. *Q. J. R. Meteorol. Soc.* (2013). doi:10.1002/qj.2063

36. Soden, B. J. *et al.* Quantifying Climate Feedbacks Using Radiative Kernels. *J. Clim.* **21**, 3504–3520 (2008).

37. Zhang, B., Kramer, R. J. & Soden, B. J. Radiative Feedbacks Associated with the Madden–Julian Oscillation. *J. Clim.* **32**, 7055–7065 (2019).

38. Kramer, R. J., Matus, A. V, Soden, B. J. & L'Ecuyer, T. S. Observation-Based Radiative Kernels From CloudSat/CALIPSO. *J. Geophys. Res. Atmos.* **124**, 5431–5444 (2019).

**Figure Legend**

Fig. 1. Time series of global mean surface temperature changes (ºC) in response to a 1% annual increase in $CO_2$ concentration for (solid) the STD and (dashed) fixed-SSS-GL version. Data are plotted as 20-year running mean.

Fig. 2. **a**. Annual series of changes in (blue) top-of-atmosphere (TOA) net radiation (W $m^{-2}$) and (red) ocean heat content (OHC; $10^{24}$ J) in response to a 1% annual increase in $CO_2$ for (solid line) the STD and (dashed line) fixed-SSS-GL version. The grey line indicates year 170 when the $CO_2$ doubles. The TOA net radiation is plotted as 10-year running mean. **b**. Difference in the response of OHC ($10^9$ J $m^{-2}$) to $CO_2$ doubling between the STD and fixed-SSS-GL version. The difference is computed using years 161-180 for the $CO_2$ run while years 101-200 for the control run. **c**. The same as **b**. but for difference in the response of sea surface salinity (SSS; psu). **d**. The linear trend of SSS (psu/50yr) from NCEI data over the period of 1968-2017. The trend is tuned by the ratio of $CO_2$ concentration at $CO_2$ doubling in FLOR to that in 2017 from observations. The area with statistical significance ($p < 0.05$) is stippled.

Fig. 3. **a**. Difference in the response of OHC ($10^{24}$ J) to transient $CO_2$ doubling between the STD and fixed-SSS-GL version as a function of ocean depth. The difference is computed using years 161-180 for the $CO_2$ run while years 101-200 for the control run. The inset figure indicates the area of Atlantic and non-Atlantic Oceans for computing total OHC. **b-c**. Difference in the response of zonal-integral **b** ocean salinity ($10^6$ psu·m; color) and **c** ocean temperature ($10^6$ ºC·m; color) between the STD and fixed-SSS-GL version in the Atlantic using the same period as **a**. **d-**

**e**. As in **b-c**, but non-Atlantic Oceans. Black lines in **b-d** indicate winter mixed layer depth (mld; m) from control runs (solid) and $CO_2$ runs (dashed), respectively. The mld in **b**, **d** are from the STD version while the mld in **c**, **e** are from the fixed-SSS-GL version.

Fig. 4. **a-b**. Change in zonal-integral **a** ocean subsurface salinity ($10^6$ psu·m; color) and **b** ocean temperature ($10^6$ $^oC$ ·m; color) in response to transient $CO_2$ doubling in the Atlantic Ocean for the STD runs. **c-d**. As in **a-b**, but non-Atlantic Oceans. **e-h**. As in **a-d**, but the linear trend of ocean salinity ($10^6$ psu·m/50yr) and temperature ($10^6$ $^oC$·m/50yr) from the NCEI data over the period of 1968-2017. The trend is tuned by the ratio of $CO_2$ concentration at $CO_2$ doubling in FLOR to that in 2017 from observations.

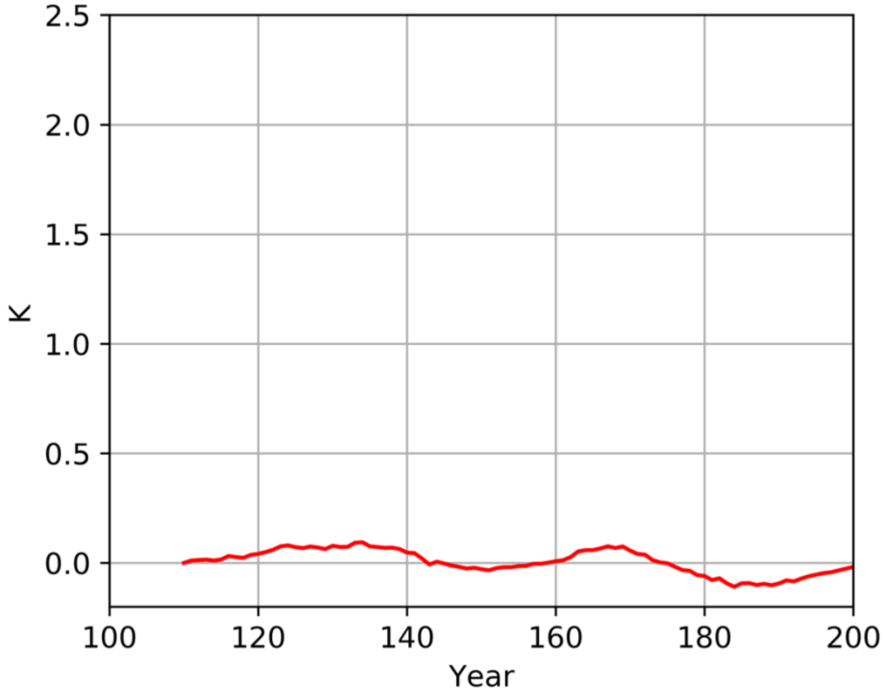


Supplementary Fig. 1. Time series of difference in global mean surface temperature (K) between the control run of the STD and fixed-SSS-GL version. Data are plotted as 20-year running mean.

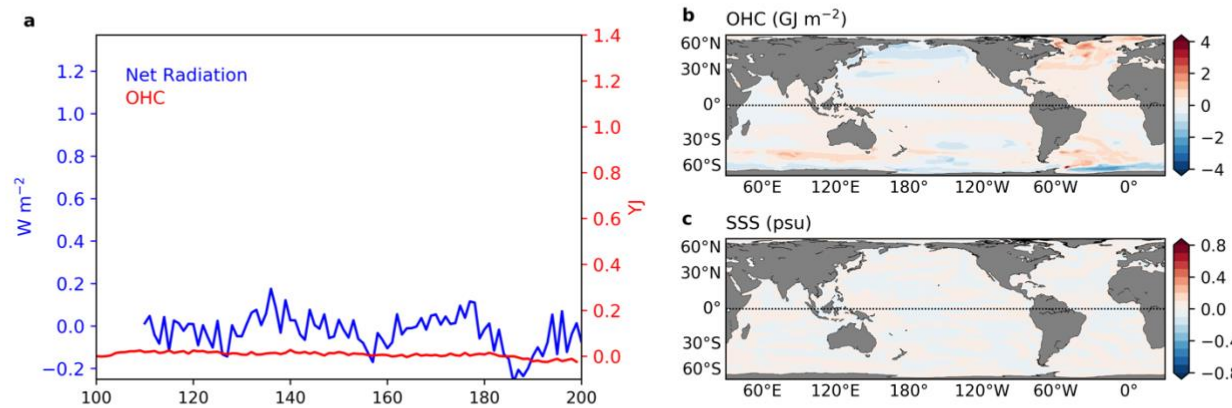


Supplementary Fig. 2. **a**. Time series of difference in global-mean the top-of-atmosphere net radiation (blue) and global-total ocean heat content change (OHC; red) between the control run of the STD and fixed-SSS-GL version. **b**. Difference in OHC climatology (GJ m$^{-2}$ or $10^9$ J m$^{-2}$) between the STD and fixed-SSS-GL version from the 100-year control run. **c**. the same as **b.** but for SSS (psu).

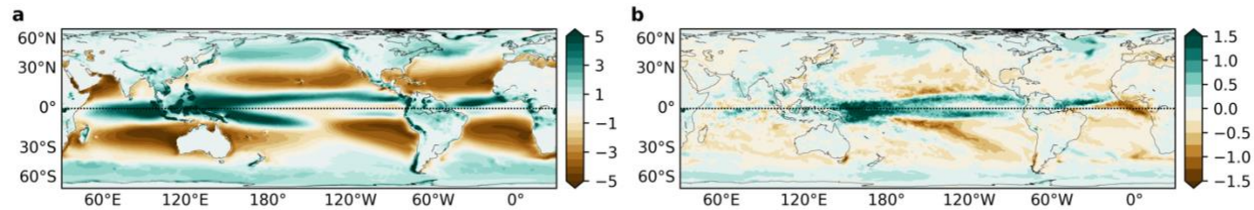


Supplementary Fig. 3. **a**. The climatology of P-E (mm $day^{-1}$) from the STD version from the 100-year control run. **b**. Change in P-E in response to the transient $CO_2$ increase for the STD version.

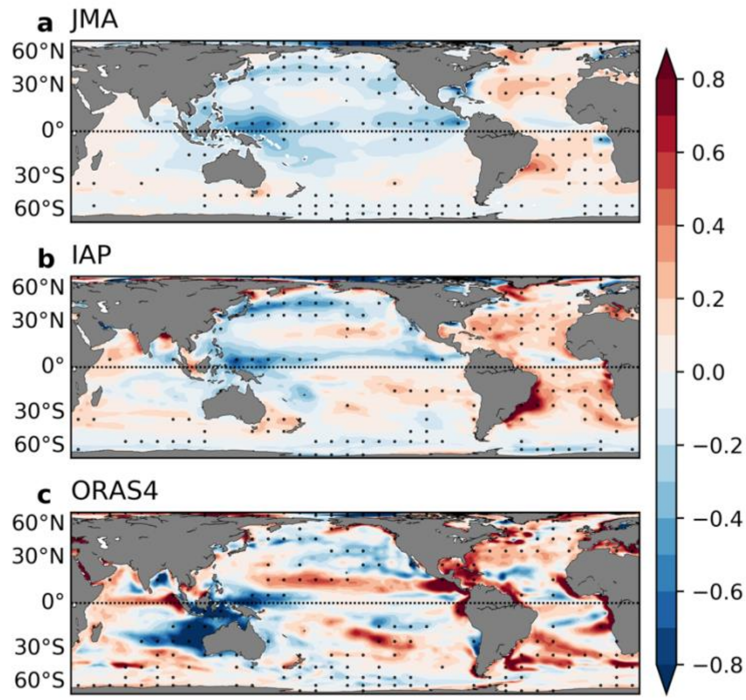


Supplementary Fig. 4. **a**. The linear trend (psu/50yr) of sea surface salinity over the period of 1968-2017 from **a** JMA, **b** IAP, and **c** ORAS4 data. The trend is tuned by the ratio of $CO_2$ concentration at $CO_2$ doubling in FLOR to that in 2017 from observations. The area with statistical significance ($p < 0.05$) is stippled.

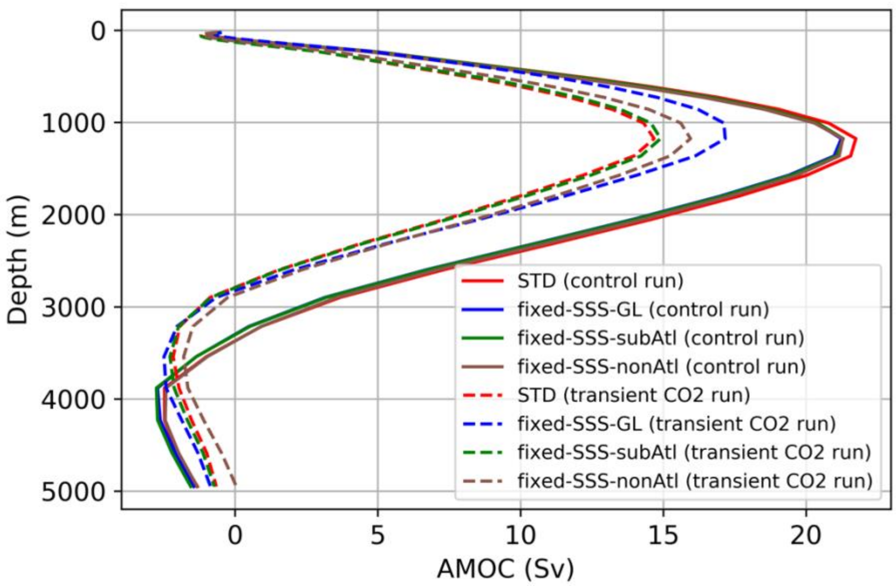


Supplementary Fig. 5. The streamfunction of AMOC (Sv) as a function of depth at 40°N for all FLOR runs. The control runs use model year 101-200 while the transient $CO_2$ runs use model years 161-180 centered on the year with $CO_2$ doubling (year 170).

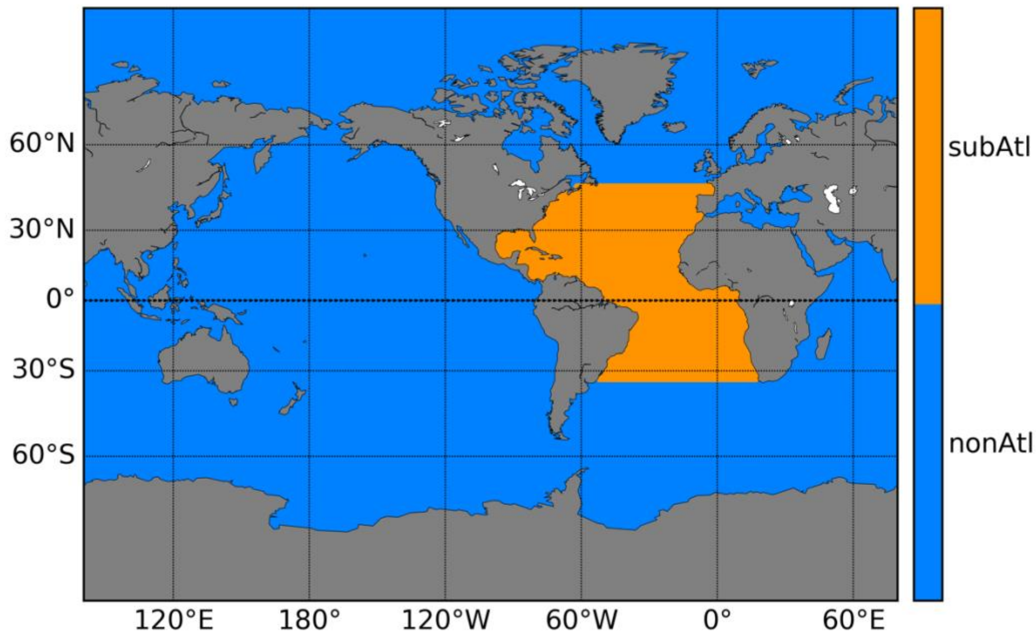


Supplementary Fig. 6. The subtropical Atlantic Ocean (masked in orange) used for the fixed-SSS-subAtl experiment.

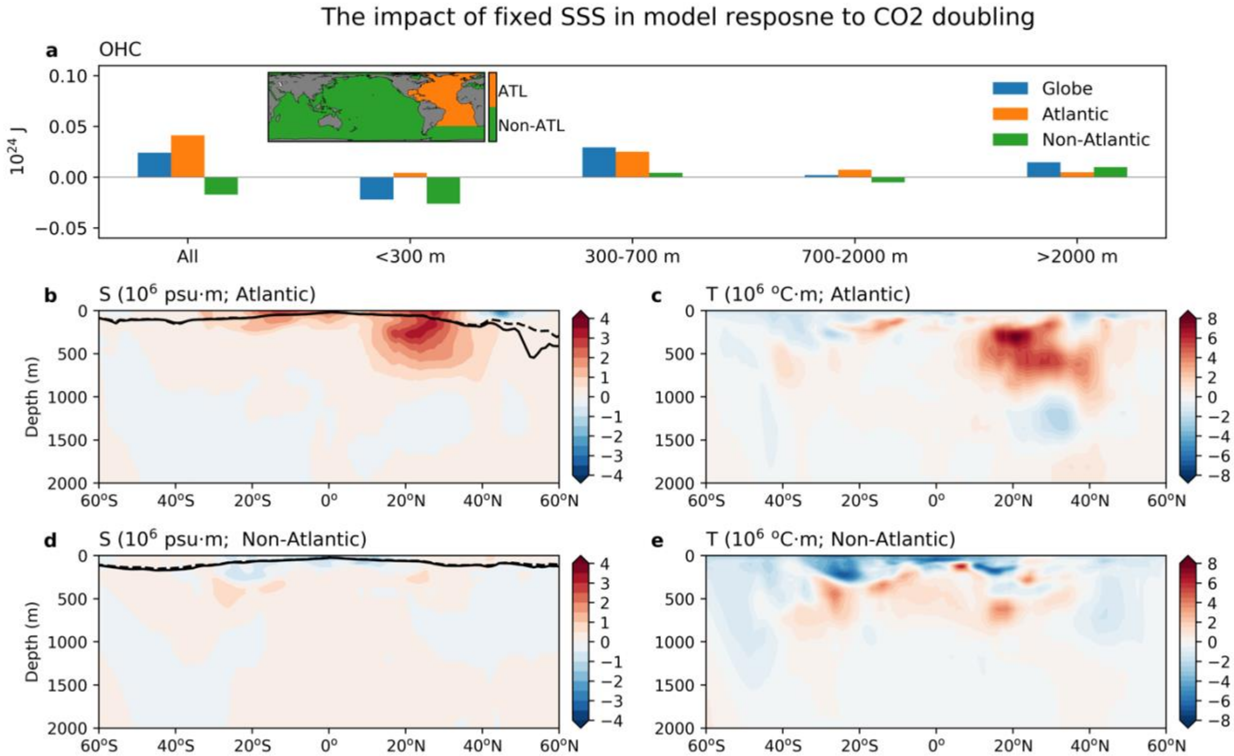


443

444 Supplementary Fig. 7. As in Fig. 3, but using the FLOR experiments with fixed SSS in the
445 subtropical Atlantic as indicated in Supplementary Fig. 6 (the fixed-SSS-subAtl version).
446

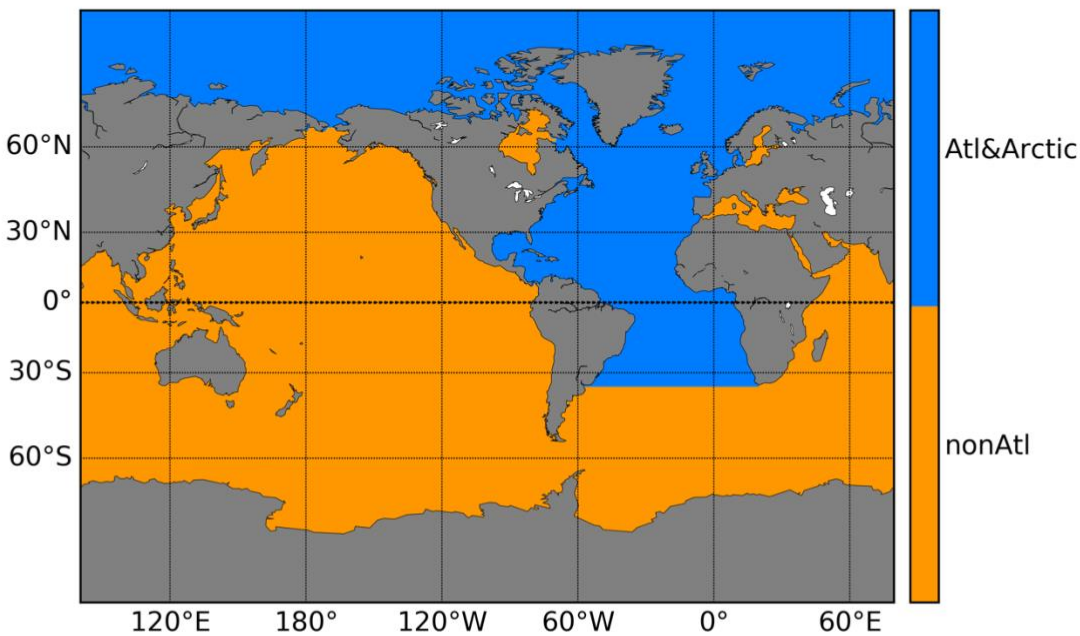


Supplementary Fig. 8. The non-Atlantic Oceans (masked in orange) used for the fixed-SSS-nonAtl experiment.

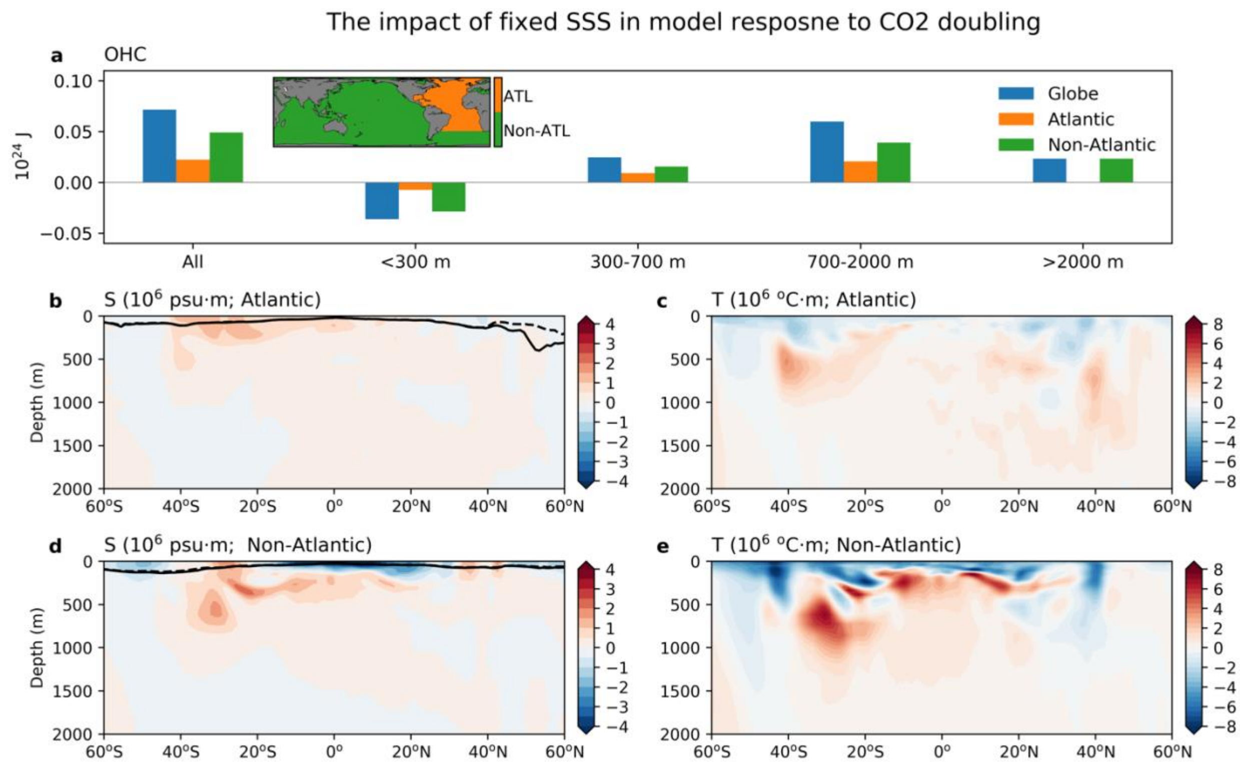


Supplementary Fig. 9. As in Fig. 3, but using the FLOR experiments with fixed SSS in the non-Atlantic as indicated in Supplementary Fig. 8 (the fixed-SSS-nonAtl version).

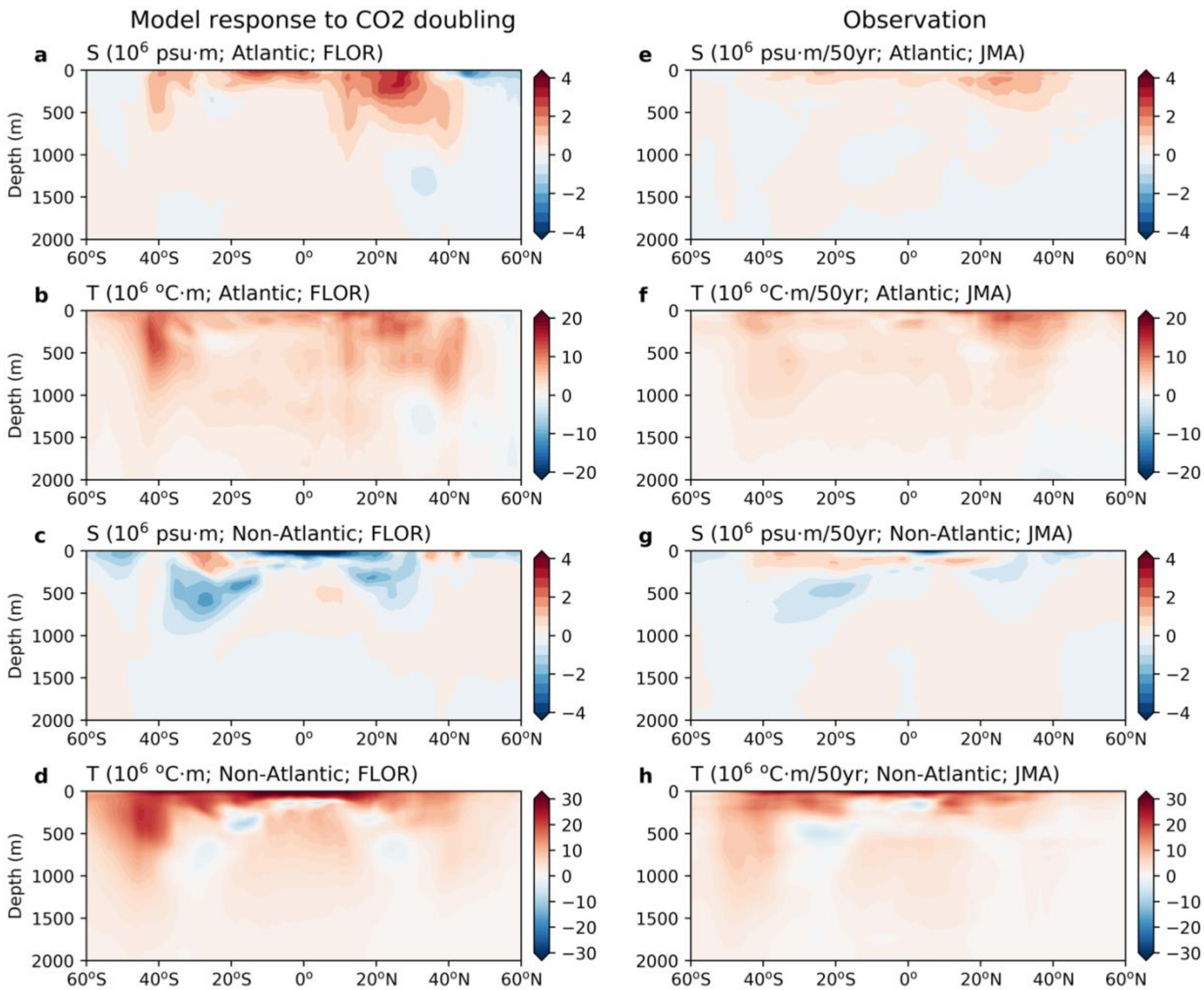


Supplementary Fig. 10. As in Fig. 4, but using JMA data.

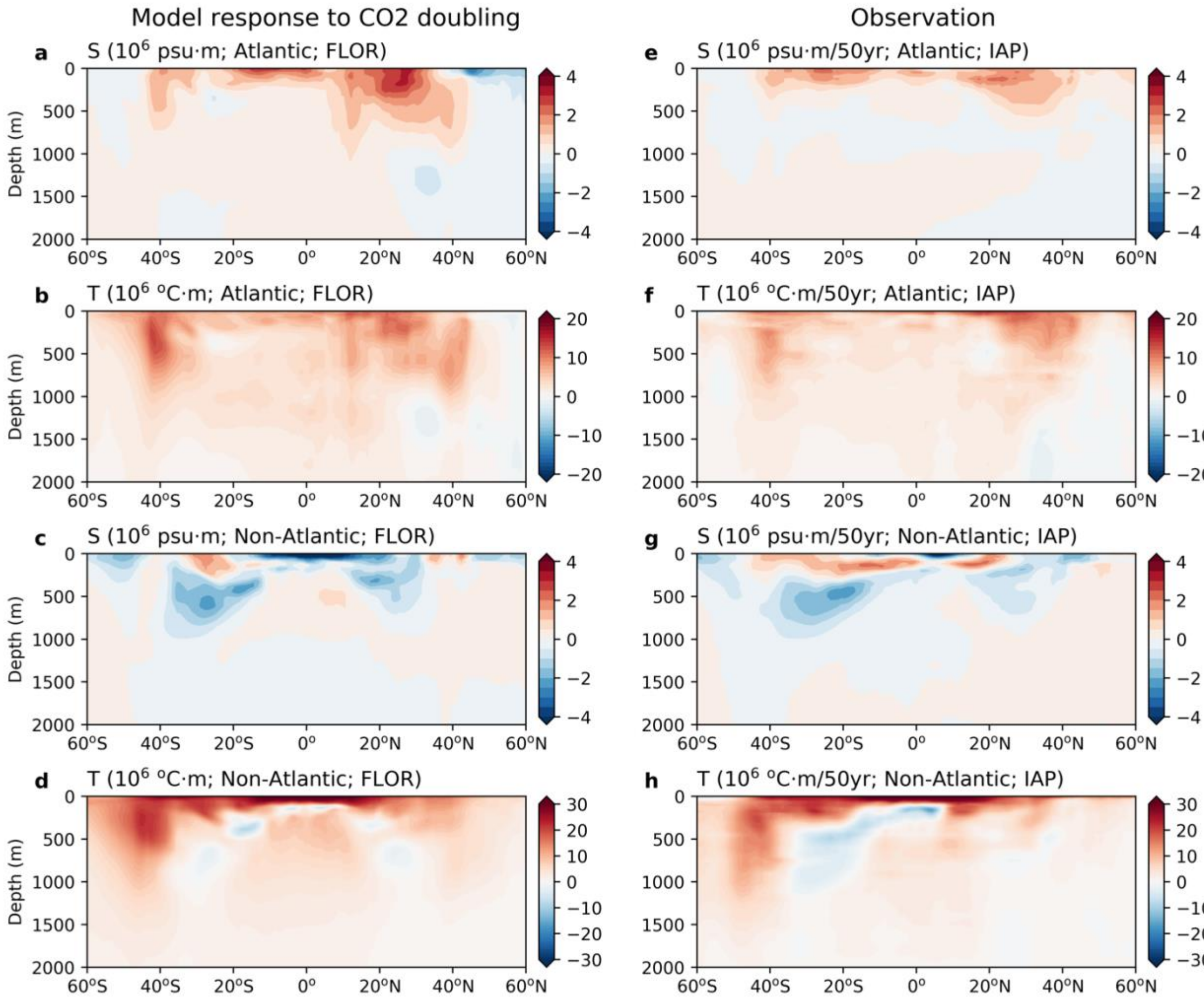


Supplementary Fig. 11. As in Fig. 4, but using IAP data.

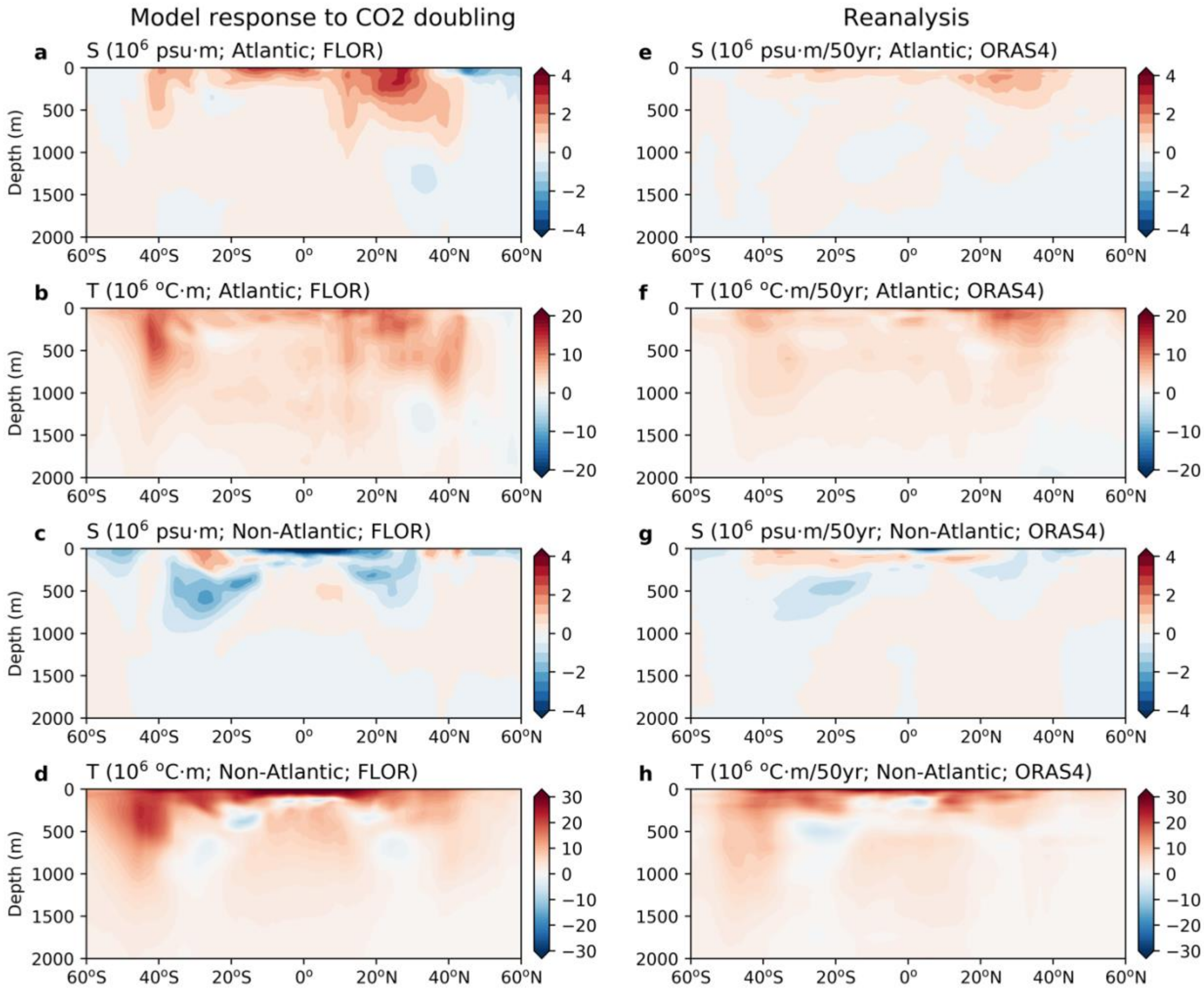


Supplementary Fig. 12. As in Fig. 4, but using ORAS4 data.